Development of a potential optical thermometric material through photoluminescence of Pr^{3+} in La_2MgTiO_6

Shi, Rui; Lin, Litian; Dorenbos, Pieter; Liang, Hongbin

DOI
10.1039/c7tc02661g

Publication date
2017

Document Version
Final published version

Published in
Journal of Materials Chemistry C: materials for optical and electronic devices

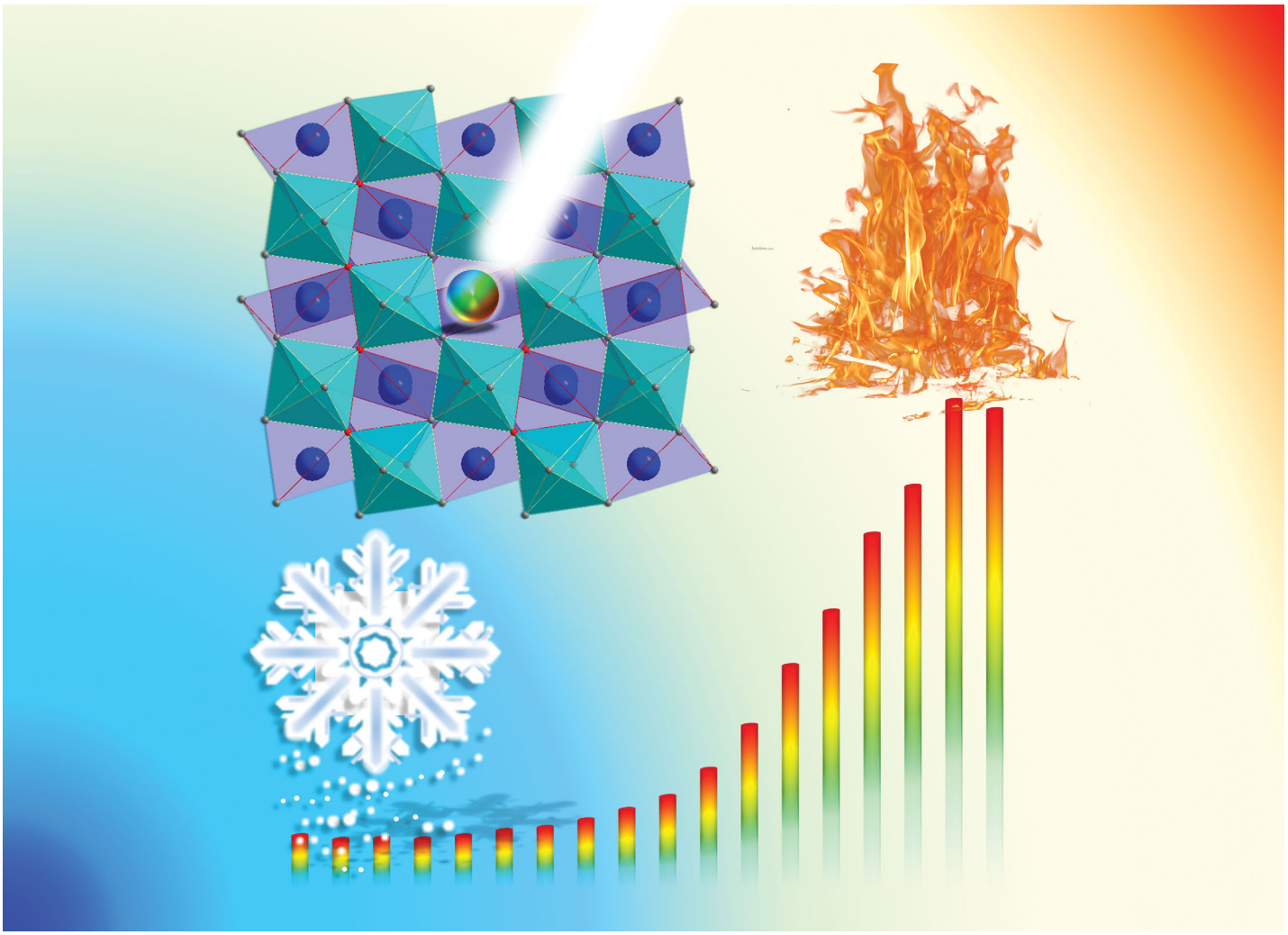

Research from the MOE Key Laboratory of Bioinorganic and Synthetic Chemistry, KLGHI of Environment and Energy Chemistry, School of Chemistry, Sun Yat-sen University.

Development of a potential optical thermometric material through photoluminescence of Pr^{3+} in La_2MgTiO_6

High-precision optical thermometric materials play a key role in controlling temperature within the non-contact situation. This research indicates that $(La_{1-x}Pr_x)_2MgTiO_6$ shows potential in the high-sensitive optical thermometry field.

As featured in:

See Hongbin Liang *et al.*, *J. Mater. Chem. C*, 2017, **5**, 10737.

ROYAL SOCIETY OF CHEMISTRY

rsc.li/materials-c

Registered charity number: 207890

Journal of Materials Chemistry C

PAPER

View Article Online
View Journal | View Issue

Cite this: J. Mater. Chem. C, 2017, 5, 10737

Development of a potential optical thermometric material through photoluminescence of Pr^{3+} in La_2MgTiO_6†

Rui Shi,[a] Litian Lin,[a] Pieter Dorenbos[b] and Hongbin Liang*[a]

Received 15th June 2017,
Accepted 16th September 2017

DOI: 10.1039/c7tc02661g

rsc.li/materials-c

In this work, we demonstrate a potential thermometric material after systematic studies on the concentration/temperature-dependent spectroscopic properties of Pr^{3+} excited multiplets and of the Pr^{3+}–Ti^{4+} intervalence charge transfer (IVCT) state in $(La_{1-x}Pr_x)_2MgTiO_6$. The experimental results indicate that the electron population efficiency between the involved Pr^{3+} 4f multiplets is directly governed by multi-phonon relaxation (MPR) and cross relaxation (CR), and the IVCT state provides an additional contribution to the $^1D_2$ luminescence. A schematic energy level diagram is proposed to illustrate the electron population pathway in Pr^{3+} doped La_2MgTiO_6. The observations clarify that the dramatic thermal-quenching of $^3P_0$ luminescence is mainly induced by the electronic configuration crossover between the $^3P_0$ multiplet and the IVCT state. On the other hand, the $^1D_2$ luminescence possesses an excellent thermal stability in a large temperature region. These temperature sensing features of the Pr^{3+} doped La_2MgTiO_6 material indicate its potential application in optical thermometric techniques.

1 Introduction

High-precision temperature sensing plays a key role in controlling the reaction process, product performance, and safety in production.[1–3] Physical probes such as thermometers and thermocouples, unfortunately, have limited utility in the situation of noncontact, small volumes, as well as high spatial resolutions, operating in hostile environments, or within dynamic systems.[4,5] Alternatively, optical thermometry acts as a feasible method benefiting from rapid-response fluorescence spectroscopy techniques. To satisfy the requirements of different technical applications, investigations on various lanthanide-doped thermometric materials have been attracting much attention recently.[6] Within the unique $4f^2$ electronic configuration, Pr^{3+} exhibits interesting properties and is widely used in lighting devices,[7] *in vivo* targeted bioimaging,[8] and up-conversion areas.[9] Upon UV or visible light excitation, Pr^{3+} usually shows bright green-bluish luminescence arising from the $^3P_0$ multiplet and red emission from the $^1D_2$ multiplet.[10] Following the SLJ transition selection rule of lanthanides in the optical material, the transition possibilities of these emissions are generally determined by the coordination environment, the spatial distribution of Pr^{3+} in the crystal structure and the vibration frequency of the host lattice.[11]

In line with other perovskites,[12] La_2MgTiO_6 is an ideal host material because of its attractive structure characteristics. The appropriate spatial distribution of La^{3+} sites in the crystal (with a two nearest La^{3+}–La^{3+} distance of about 3.9384 Å) is in favour of investigating the correlation between the luminescence of Pr^{3+} 4f excited multiplets and doping concentration. Due to the proper Pr^{3+}–Ti^{4+} distance (3.3054 Å), the Pr^{3+}–Ti^{4+} intervalence charge transfer (IVCT) state in the studied compound will have an impact on the electron population of the Pr^{3+} intrinsic 4f electronic configuration and further improve the light absorption efficiency of materials in the UV-vis region.

In this work, the correlations between the Pr^{3+} luminescence properties and structural factors are discussed in different doping concentration samples at different temperatures. A schematic energy level diagram is proposed to illustrate the electron population pathway and explain the thermal-quenching mechanism of Pr^{3+} luminescence. In view of the different thermal-quenching behaviours of $^3P_0$ and $^1D_2$ luminescence, the possible thermometric application of Pr^{3+} doped La_2MgTiO_6 is demonstrated.

2 Experimental section

A series of Pr^{3+} doped La_2MgTiO_6 was prepared using a high temperature solid-state reaction route. The details of the preparation and measurements are described in the ESI.†

[a] MOE Key Laboratory of Bioinorganic and Synthetic Chemistry, KLGHI of Environment and Energy Chemistry, School of Chemistry, Sun Yat-sen University, Guangzhou 510275, China. E-mail: cesbin@mail.sysu.edu.cn; Fax: +86 20 84111038; Tel: +86 20 84113695

[b] Faculty of Applied Sciences, Delft University of Technology, Mekelweg 15, 2629 JB Delft, The Netherlands

† Electronic supplementary information (ESI) available. See DOI: 10.1039/c7tc02661g

3 Results and discussion

3.1 Structure Characteristics

The Rietveld structure refinement of high-quality powder XRD data of La_2MgTiO_6 was performed using the TOPAS program.[13] Fig. 1(a) represents the experimental XRD pattern (×), the refinement result (red line), the difference (blue line) and the calculated Bragg positions (|) of La_2MgTiO_6. The values of the fitting parameters R_p and R_{wp} are within the rational range, indicating that the refinement results are reliable. La_2MgTiO_6 has a double-perovskite structure and there are two different types of cation sites: (A) La^{3+} sites coordinated with twelve oxygen atoms with C_s symmetry; (B) Ti^{4+}/Mg^{2+} mix-occupied sites with six-fold coordination. The Ti^{4+}/Mg^{2+}–O^{2-} octahedra link with each other by corner-sharing, and La^{3+} is located in the cavity with the surrounding eight Ti^{4+}/Mg^{2+}–O^{2-} octahedra as shown in the inset. Refined atom positions and unit cell parameters are listed in Table S1, and the refined bond lengths are listed in Table S2 (ESI†). The distance between the two nearest neighbour La^{3+} ions is 3.9384 Å, and the nearest La^{3+}–Ti^{4+}/Mg^{2+} distance is 3.3054 Å. The average La^{3+}–O^{2-} and Ti^{4+}/Mg^{2+}–O^{2-} bond lengths are 2.7966 and 2.0073 Å, respectively. In consideration of the larger ionic radius differences between Ti^{4+}/Mg^{2+} and Pr^{3+}, the dopants preferably occupy La^{3+} sites because of the similarity in the ionic radii (La^{3+}:1.320 Å; Pr^{3+}:1.286 Å, when the coordination number (CN) = 6).[14]

Fig. 1(b) shows the variations of the unit cell parameters with the increase in Pr^{3+} content at RT. The values of *a*, *b* and *c* decrease with an increase in the doping content, indicating the gradual lattice contraction. In consideration of the ionic radius difference (0.034 Å) of La^{3+} and Pr^{3+}, such a decrease in the parameter values is expected. Fig. 1(c) exhibits the cell parameters at different temperatures, which indicates that expansion of the host lattice is induced by increasing temperatures.

Fig. S1 (ESI†) shows the FT-IR spectra of the host compound and $(La_{0.95}Pr_{0.05})_2MgTiO_6$ samples at RT. Two absorption bands are spread over the region of 400–700 cm^{-1} with maxima at 420 and 585 cm^{-1}. The former is attributed to Ti–O–Ti bending vibration modes and the latter is assigned to Ti–O stretching vibrations in TiO_6 polyhedra, respectively.[15]

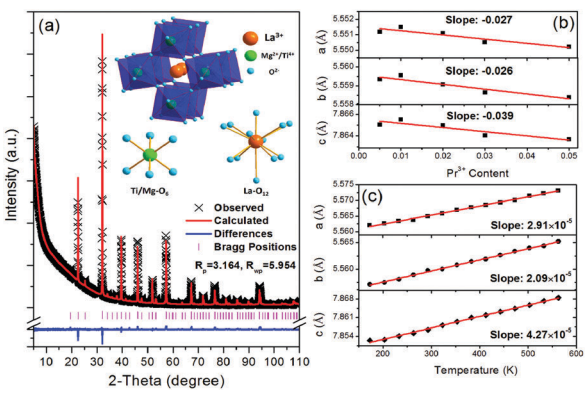

Fig. 1 (a) The Rietveld refinement fit of the La_2MgTiO_6 experimental XRD pattern by the TOPAS program; (b) the variations of lattice parameters (*a*, *b* and *c*) of $(La_{1-x}Pr_x)_2MgTiO_6$ with different Pr^{3+} contents; (c) the variations of lattice parameters of La_2MgTiO_6 at different temperatures.

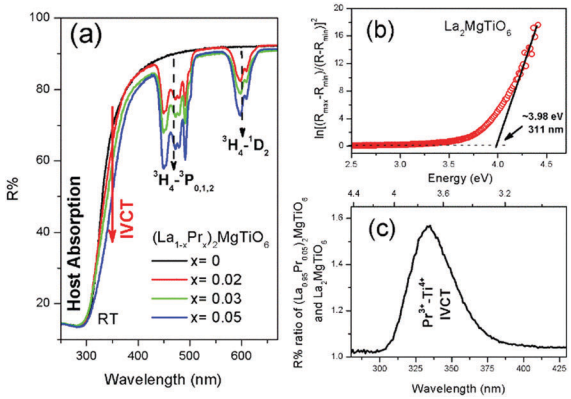

Fig. 2 (a) Diffuse reflectance spectra (DRS) of $(La_{1-x}Pr_x)_2MgTiO_6$ (x = 0, 0.02, 0.03, 0.05) samples at RT; (b) the plot of $\{\ln[(R_{max} - R_{min})/(R - R_{min})]\}^2$ *vs.* energy (eV) where R is reflectance; (c) the difference between the DRS of $(La_{0.95}Pr_{0.05})_2MgTiO_6$ and La_2MgTiO_6 in the wavelength region 280–430 nm.

3.2 Diffuse reflectance spectra (DRS) of $(La_{1-x}Pr_x)_2MgTiO_6$

Diffuse reflectance spectra (DRS) of the $(La_{1-x}Pr_x)_2MgTiO_6$ (x = 0, 0.02, 0.03 and 0.05) samples at RT are exhibited in Fig. 2(a). All samples show strong host absorption in the short-wavelength (300–400 nm) region. This is attributed to the electronic transition from the valence band (VB) maximum to the conduction band (CB) minimum of the energy band structure, which are mainly constructed by the ligand (like O^{2-}) 2p orbital and the central cation (like Ti^{4+}, Mg^{2+}, and La^{3+}) higher electronic states, respectively. The optical band gaps of several titanates have been reported to be: 3.9 eV ($NaGdTiO_4$),[15] 3.85 eV ($CaTiO_3$),[16] and 3.8 eV ($La_2Ti_2O_7$).[17] By adopting the method of Kumar *et al.*,[18] the optical band gap of La_2MgTiO_6 is determined to be 3.98 eV as plotted in Fig. 2(b). After incorporation of Pr^{3+} in La_2MgTiO_6, several absorption lines of Pr^{3+} 4f–4f transitions are observed, which are attributed to the $^3H_4$–$^3P_{0,1,2}$, $^1I_6$ (450–500 nm) and the $^3H_4$–$^1D_2$ (580–630 nm) transitions, respectively. The absorption strength of these lines increases with the increase in the Pr^{3+} content. Another broad absorption appears in the 320–430 nm wavelength region and its absorption strength gradually increases with increasing Pr^{3+} content (indicated by a red arrow). This band results from the Pr^{3+}–Ti^{4+} IVCT, and corresponds to the electron transition from the Pr^{3+} $^3H_4$ ground state to the unoccupied $3d^1$ orbital of Ti^{4+}.[19] Because of the considerable overlap with the host absorption, the IVCT band cannot be separately observed in DRS. The difference between the DRS of $(La_{0.95}Pr_{0.05})_2MgTiO_6$ and La_2MgTiO_6 in the wavelength region 280–430 nm is shown in Fig. 2(c) by dividing the diffuse reflectance of $(La_{0.95}Pr_{0.05})_2MgTiO_6$ by that of La_2MgTiO_6. A broad band is clearly observed in the spectrum with the energy maximum at 3.71 eV (335 nm, 29.8 × 10^3 cm^{-1}). When we assume that the two samples $(La_{0.95}Pr_{0.05})_2MgTiO_6$ and La_2MgTiO_6 have nearly the same host-related diffuse reflection strength in this

region, the band in Fig. 2(c) corresponds to the Pr^{3+}–Ti^{4+} IVCT absorption of $(La_{0.95}Pr_{0.05})_2MgTiO_6$.

Boutinaud *et al.*[19] have proposed an empirical relationship (eqn (1)) to estimate the IVCT energy in Pr^{3+} doped titanates:

$$\mathrm{IVCT}(\mathrm{cm}^{-1}) = 58\,800 - 49\,800\left[\frac{\chi(\mathrm{Ti}^{4+})}{d(\mathrm{Pr}^{3+}-\mathrm{Ti}^{4+})}\right] \quad (1)$$

where $\chi(Ti^{4+})$ is the optical electronegativity (2.05) of Ti^{4+}, and $d(Pr^{3+}$–$Ti^{4+})$ is the average distance between the neighbouring Pr^{3+} and Ti^{4+} (Å). In La_2MgTiO_6, $d(Pr^{3+}$–$Ti^{4+})$ is obtained from the crystal refinement result (3.3054 Å), therefore the IVCT energy is approximately 28.0×10^3 cm^{-1} (3.57 eV), which is consistent with the result (29.8×10^3 cm^{-1}, 3.36 eV) estimated from the experimental data.

3.3 Luminescence of $(La_{0.9975}Pr_{0.0025})_2MgTiO_6$

The 3D colour-filled contour map of the time-resolved emission spectra (TRES) of $(La_{0.9975}Pr_{0.0025})_2MgTiO_6$ under 450 nm excitation at RT is given in Fig. 3(a), and the emission spectra of the sample at different delay times are displayed in b1–b4, respectively. Because of the distinct types of transitions arising from the $^3P_0$ and $^1D_2$ multiplets following the SLJ transition selection rule, these emissions have different time-dependent decay properties. Within the short delay time t_{delay} ~15.6 μs, several emission lines are detected in spectrum b1, which are mainly assigned to transitions arising from the $^3P_0$ multiplet. When t_{delay} is 18 μs, the emission intensity of $^3P_0$ increases to the maximum, and further increase in t_{delay} results in a rapid drop of the $^3P_0$ emission intensity. No significant $^1D_2$–$^3H_4$ emission can be observed in this time region, which implies that after excitation to the $^3P_0$ level the rate of radiative emission from the $^3P_0$ multiplet is significantly higher than that of the nonradiative population from the $^3P_0$ to $^1D_2$ multiplets. With a gradual rise in t_{delay} to 60 μs, the $^3P_0$ emissions decay to a comparable intensity relative to the intensity of $^1D_2$ emission because the faster emissions arising from $^3P_0$ are spin-allowed, but the slower $^1D_2$–$^3H_4$ transition is spin-forbidden. This is because the emission of $^1D_2$ emerges in the spectrum and its contribution becomes comparable to that of $^3P_0$ emission. When t_{delay} increases to 120 μs, the $^1D_2$–$^3H_4$ emission is predominant, and the contribution of $^3P_0$ emission is negligible. Fig. S2 (ESI†) represents decay curves of the $^3P_0$ and $^1D_2$ multiplets in $(La_{0.9975}Pr_{0.0025})_2MgTiO_6$ under 450 nm excitation at RT. Both curves obey the exponential characteristic and decay times of the $^3P_0$ and $^1D_2$ multiplets which are estimated to be ~4.3 and 56.6 μs, respectively. Correspondingly, the radiative transition rate (A_R) values of the $^3P_0$ and $^1D_2$ multiplets are evaluated to be approximately 2.3×10^5 s^{-1} and 1.7×10^4 s^{-1} at RT.

Fig. 4 shows the excitation spectra of $(La_{0.9975}Pr_{0.0025})_2MgTiO_6$ with different emission wavelengths at RT. All spectra are normalized to the height of the broad excitation band in the short wavelength region. As displayed in Fig. 4(a1), when monitoring the 490 and 651.5 nm emissions of the Pr^{3+} $^3P_0$ multiplets, a weak but broad absorption band is found in the short-wavelength region, and some intense sharp excitation lines identified as the $^3H_4$–$^3P_{0,1,2}$ and $^1I_6$ transitions are observed in the longer wavelengths (>425 nm). The relative intensity of the Pr^{3+} f–f transition is predominant in the spectrum, indicating that the electron population from Pr^{3+} higher 4f multiplets to $^3P_0$ is efficient. By changing the monitored emission wavelength to 608 nm of the $^1D_2$ emission as exhibited in Fig. 4(a2), the relative height of the broad absorption becomes higher than those of 4f–4f transitions, showing an indispensable contribution of this broad band to the emission from $^1D_2$. The enlargement of the broad bands in excitation spectra a1 and a2 is shown in Fig. 4(b). The two height-normalized broad bands of 490 and 651.5 nm $^3P_0$ emissions almost overlap, but the band maximum shows a red-shift when monitoring 608 nm $^1D_2$ emission. In terms of DRS, the absorptions in this region contain host absorption and the Pr^{3+}–Ti^{4+} IVCT band, and the red-shift should result from the contribution of the IVCT transition.

Fig. 5 represents emission spectra under (a1) 450/490 nm, (a2) 335 nm and (a3) 310 nm excitations at RT, respectively. Under 450/490 nm $^3H_4$–^3P_J (J = 0, 2) excitations, the emission coming from the $^3P_0$ multiplet is predominant and the induced electric-dipole (ED) $^3P_0$–$^3F_2$ transition (hypersensitive, $\Delta S = 0$ and $\Delta J = 2$)

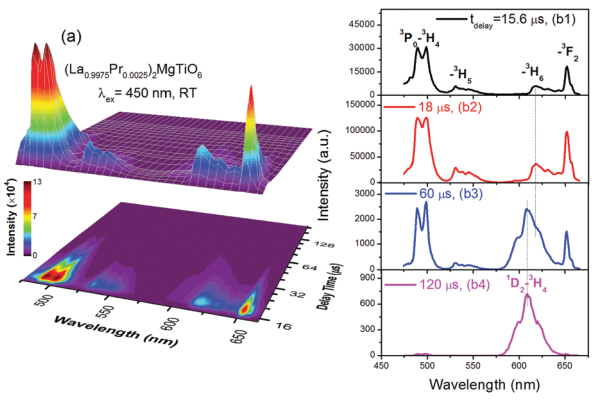

Fig. 3 (a) The 3D colour-filled contour map of the time-resolved emission spectra (TRES) of $(La_{0.9975}Pr_{0.0025})_2MgTiO_6$ under 450 nm excitation at RT; the specific emission spectra of the sample at different delay times are given in b1–b4, respectively.

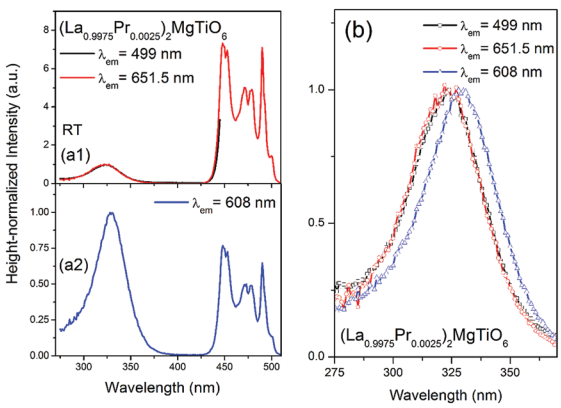

Fig. 4 The height-normalized excitation spectra of $(La_{0.9975}Pr_{0.0025})_2MgTiO_6$ with (a1) 499 and 651.5 nm and (a2) 608 nm emissions at RT; (b) the enlargement of the broad bands in the region of 265–375 nm of (a).

with the maximum at 651.5 nm is clearly observed. In most cases the $^3P_0$–$^3H_4$ transition is stronger than the $^3P_0$–$^3F_2$ transition after excitation to the $^3P_0$ level,[20] but exceptional cases have also been reported in Pr^{3+} doped $Na_2La_2Ti_3O_{10}$,[21] $LaMgAl_{11}O_{19}$,[22] and $KLa(MoO_4)_2$.[23] Cavalli *et al.*[24] have mentioned that the intense $^3P_0$–$^3F_2$ radiative transition rate is closely related to the large value of the Judd–Ofelt Ω_2 parameter in the lattice. Further investigations demonstrate that a large value of the Ω_2 parameter is associated with a stronger polarization effect of the ligands in medium and the first-order terms of the crystal field strength around the central lanthanides.[25,26] In addition, a predominant $^3P_0$–$^3F_2$ transition has also been observed in Pr^{3+} doped compounds with general covalence when Pr^{3+} ions occupy lattice sites with obvious deviation from centrosymmetry.[22] In La_2MgTiO_6, the La^{3+} site exhibits C_s symmetry that is far deviated from centrosymmetry, therefore the intense $^3P_0$–$^3F_2$ transition is to be expected.

On changing the excitation to 335 nm (the IVCT), a remarkable increase in the relative emission intensity of the $^1D_2$–$^3H_4$ transition is observed and the contribution of $^1D_2$ emission in the spectrum is dominant. This phenomenon is in good agreement with the results of the excitation spectra in Fig. 4, and implies that the electrons in the IVCT state preferentially populate $^1D_2$ and partially bypass the $^3P_0$ multiplet.[19] With further change in the excitation to the host absorption at 310 nm (a3), the $^3P_0$ emission intensity becomes slightly larger compared to that under IVCT excitation, demonstrating that the de-excitation pathway after host absorption excitation may be somewhat different from that after excitation to the IVCT state.

A schematic energy level diagram is proposed in Fig. 5(b) to illustrate the electron population pathway in Pr^{3+} doped La_2MgTiO_6. Under 335 nm IVCT excitation, the electron in the Pr^{3+} $^3H_4$ ground state is transferred to the Ti^{4+} orbital, and the $[Ti^{4+} + e^-]$ state (such as the IVCT state as mentioned above) is created.[27] After fast non-radiative relaxation, the electron returns to the minimum potential energy position of the $[Ti^{4+} + e^-]$ state (point A) and rapidly transfers to the Pr^{3+} 4f excited multiplets (like the $^3P_0$, $^1D_2$) with the assistance of thermal phonons creating the observed 4f–4f emission lines in the spectrum. Because the energy barrier between the $[Ti^{4+} + e^-]$ state and the $^3P_0$ multiplet (ΔE_{AC}) is evidently larger than that between the $[Ti^{4+} + e^-]$ state and the $^1D_2$ multiplet (ΔE_{AB}), the electron preferably populates the $^1D_2$ multiplet (pathway 1), and the $^1D_2$ emission is dominant in the spectrum under IVCT excitation as shown in Fig. 5(a2). After populating the CB upon 310 nm host absorption excitation, the electrons relax to the IVCT and the $^3P_0$ states simultaneously with different non-radiative rates. This means that the Pr^{3+} $^3P_0$ excited state can also be directly populated from the CB. Accordingly, the relative contribution of $^3P_0$ emission under 310 nm excitation is larger than that under 335 nm excitation. In the following discussions, we choose 350 nm as the IVCT excitation wavelength to avoid the co-excitation of host absorption and the IVCT, and the emission spectrum of the sample under 350 nm excitation is shown in Fig. 5(a4).

3.4 Concentration-dependent luminescence of $(La_{1-x}Pr_x)_2MgTiO_6$

Fig. 6 shows the 3D colour-filled contour map of the normalized excitation spectra of $(La_{1-x}Pr_x)_2MgTiO_6$ (x = 0.0025–0.05) when monitoring 608 nm emission at RT. To discuss the influence of the doping content on the position of the IVCT band, the relative intensity and energy maximum of host absorption are roughly regarded to be independent of the doping content. With the increase in the Pr^{3+} content, the relative intensity of the IVCT band decreases gradually along with the increase in the Pr^{3+} 4f–4f transition relative intensity. The essence of this distinction is considered as the saturation effect of photon absorptivity.[28]

Fig. 7(a) depicts the normalized emission spectra of $(La_{1-x}Pr_x)_2MgTiO_6$ (x = 0.0025–0.05) under 490 nm $^3H_4$–$^3P_0$ excitation. The spectra almost overlap with each other except for the slight decrease in weaker $^1D_2$ emission at around 600 nm. The concentration-dependence of $^3P_0$ luminescence intensity under 490 nm excitation is shown in Fig. 7(b). The integral emission intensity increases initially to the maximum at x = 0.01 and then decreases gradually with further increasing content. This indicates that the concentration-quenching of the

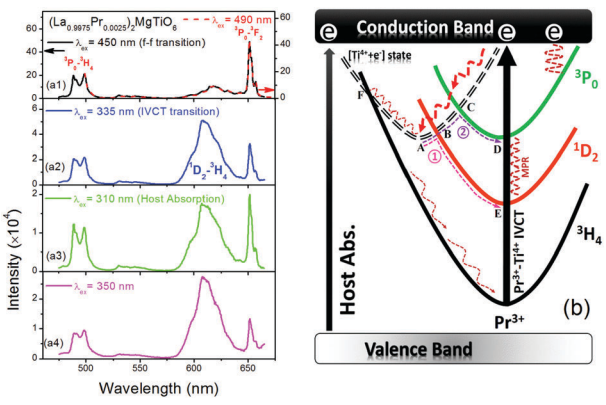

Fig. 5 The emission spectra of $(La_{0.9975}Pr_{0.0025})_2MgTiO_6$ under (a1) 450 and 490 nm, (a2) 335 nm, (a3) 310 nm, and (a4) 350 nm excitations at RT; (b) the schematic energy level diagram and electron population mechanism proposed to explain the difference in spectra.

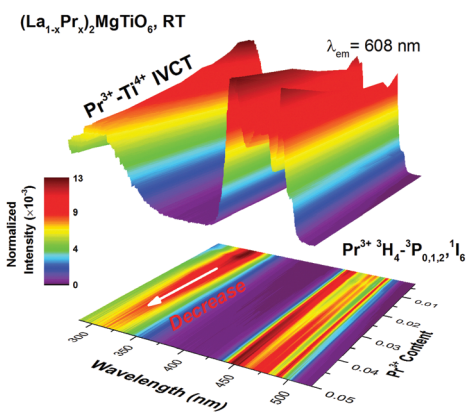

Fig. 6 The 3D colour-filled contour map of the normalized excitation spectra of $(La_{1-x}Pr_x)_2MgTiO_6$ (x = 0.0025–0.05) with 608 nm emission at RT.

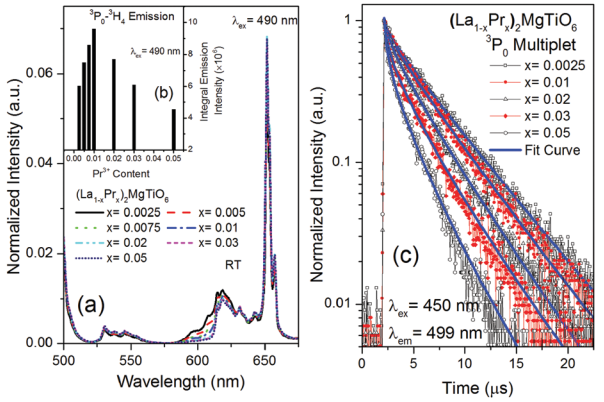

Fig. 7 (a) The normalized emission spectra of $(La_{1-x}Pr_x)_2MgTiO_6$ (x = 0.0025–0.05) under 490 nm excitation; (b) the concentration-dependence of $^3P_0$ luminescence intensity under 490 nm excitation; (c) decay dynamics of Pr^{3+} $^3P_0$ emission in $(La_{1-x}Pr_x)_2MgTiO_6$ with different doping contents at RT and the fitting results.

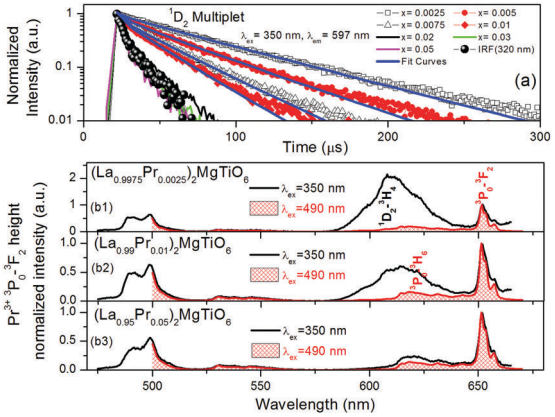

Fig. 8 (a) Decay dynamics of Pr^{3+} $^1D_2$ emission under IVCT excitation in samples with different doping contents at RT and the fit curves; (b) the height-normalized emission spectra of representative $(La_{1-x}Pr_x)_2MgTiO_6$ (x = 0.0025, 0.01, 0.05) samples under 350 and 490 nm excitations at RT, respectively.

$^3P_0$ luminescence occurs when the doping content is above x = 0.01. Decay dynamics of the $^3P_0$ emission in $(La_{1-x}Pr_x)_2MgTiO_6$ at RT is shown in Fig. 7(c). The decay curves gradually deviate from the exponential with increasing contents from x = 0.0025 to 0.05. It demonstrates that a faster non-radiative relaxation process for electrons in the $^3P_0$ multiplet becomes more active. Because of the identical ambient temperature, the contribution of multi-phonon relaxation (MPR) is negligible. We consider that this decay deviation is mainly caused by cross relaxation (CR) between the neighbouring Pr^{3+} ions. With the increase in the doping content, the distance between the adjacent Pr^{3+} becomes shorter gradually, resulting in a more efficient multipolar–multipolar interaction. Two candidate CR channels have been mentioned in references: $[^3P_0, {}^3H_4] \rightarrow [^1D_2, {}^3H_6]$ and $[^3P_0, {}^3H_4] \rightarrow [^1G_4, {}^1G_4]$. The energy difference of the former channel is $\sim$500 cm^{-1} (in LaOCl:Pr^{3+} [29]) and $\sim$1000 cm^{-1} (in $La_{0.97}Pr_{0.03}MgAl_{11}O_{19}$ [22]), and that of the latter is $\sim$265 cm^{-1} (in LaF_3:Pr^{3+} [22]). Usually, a smaller energy mismatch of the relevant energy levels would result in more efficient CR at a certain temperature. These data suggest that the electrons in the $^3P_0$ multiplet would preferably follow the $[^3P_0, {}^3H_4] \rightarrow [^1G_4, {}^1G_4]$ channel and populate the $^1G_4$ multiplet through an increasingly stronger CR process. Herein, the Inokuti–Hirayama model[30] is employed to simulate this CR process:

$$I(t) = I(0)\exp\left(-\frac{t}{\tau_0} - Q\cdot t^{\frac{3}{s}}\right)$$

$$Q = \frac{4\pi}{3}\Gamma\left(1-\frac{3}{s}\right)\cdot C_A\cdot\left(C_{DA}^{(s)}\right)^{\frac{3}{s}} \quad (2)$$

$$P_{SA} = \frac{C_{DA}^{(s)}}{R_{SA}^{s}}$$

where S determines the type of multipolar effect; C_{DA} is the kinetic micro-parameter; and P_{SA} represents the energy-transfer rate. The physical meanings of the other parameters in the equation have been described elsewhere in detail.[28] The dominant multipolar mechanism is determined to be dipole–dipole interaction and the value of C_{DA} is $\sim 7.4\times10^{-48}$ m^6 s^{-1}. Moreover, the critical doping content (x_c) and critical distance (R_c) are x = 0.014 and 20.2 Å, respectively. This critical quenching concentration is consistent with the experimental result of the $^3P_0$ luminescence.

Fig. 8(a) shows the decay dynamics of the $^1D_2$ emission under IVCT excitation in samples with different doping contents at RT. Decay curves deviate from the exponential gradually with the increase in Pr^{3+} content. The major CR channel for electrons in the $^1D_2$ multiplet is attributed to $[^1D_2, {}^3H_4] \rightarrow [^1G_4, {}^3F_4]$, and its energy mismatch ($\sim$12 cm^{-1} in LaP_5O_{14}:Pr^{3+} [31]) is quite small. Herein, the multiplet mechanism of this CR is confirmed to be a dipole–quadrupole interaction and the value of C_{DA} is evaluated to be $\sim 4.77\times10^{-64}$ m^8 s^{-1}. The values of x_c and R_c for this pathway are about x = 0.0023 and 36.9 Å, which is consistent with the results in other Pr^{3+} doped compounds.[31] Fig. 8(b) depicts the height-normalized emission spectra of representative $(La_{1-x}Pr_x)_2MgTiO_6$ (x = 0.0025, 0.01, 0.05) samples under 350 and 490 nm excitation at RT, respectively. All spectral data are normalized to the emission height at 651.5 nm of the $^3P_0$–$^3F_2$ emission. Three evident spectroscopic characteristics are found. Firstly, the emission peak in the 588–640 nm region shows a slight long-wavelength shift upon 490 nm excitation in comparison with that upon 350 nm. The emissions in this region usually contain the $^1D_2$–$^3H_4$ emission on the short wavelength and the $^3P_0$–$^3H_6$ emission on the long wavelength as mentioned in Fig. 3(b). The observed peak shift is the result of different contributions of two types of emissions under different excitations. Secondly, the $^1D_2$ emission intensity under 490 nm excitation is weaker than that under IVCT excitation in each case. Usually, the $^1D_2$ multiplet can be populated through MPR and CR processes after excitation to the $^3P_0$ state. The stronger $^1D_2$ emission means that the $^1D_2$ multiplet can be populated through an extra channel under 350 nm IVCT excitation.[19] Thirdly, the intensity difference in $^1D_2$ emission under 350 and 490 nm excitation decreases with the increase in concentration. This is mainly the result of concentration-quenching of the $^1D_2$ luminescence. Due to the

small energy mismatch of the $^1D_2$-involved CR process, concentration-quenching of $^1D_2$ is indeed prior to that of $^3P_0$.[22]

3.5 Temperature-dependent luminescence and thermometric properties of $(La_{0.9975}Pr_{0.0025})_2MgTiO_6$

Upon 350 nm excitation, Pr^{3+} 4f excited $^3P_0$ and $^1D_2$ multiplets are populated after the nonradiative relaxation from the IVCT state as shown in Fig. 5(b) and are described in Section 3.3. This is followed by emissions from the $^3P_0$ and $^1D_2$ states. Fig. 9(a) represents the emission spectra of $(La_{0.9975}Pr_{0.0025})_2MgTiO_6$ under 350 nm excitation at different temperatures. The temperature-dependences of the integral emission intensities of the $^3P_0$–$^3H_4$ and the $^1D_2$–$^3H_4$ transitions are shown in Fig. 9(b). At low temperatures (<225 K), the emission intensities arising from $^3P_0$ and $^1D_2$ multiplets are almost constant. With the increase in temperature to 500 K, the intensity of $^3P_0$ emission drops rapidly to 4.4% when compared to that at 77 K as displayed in curve b1. In contrast, the intensity of the $^1D_2$–$^3H_4$ transition increases gradually with the increase in temperature from 225 to 400 K and then slightly decreases when the temperature increases to 500 K as shown in curve b2.

Thermal-quenching behaviour of the $^3P_0$ luminescence is controlled by: (1) phonon-assisted CR; (2) MPR; and (3) electron population through electronic configuration crossover. Firstly, it is expected that the efficiency of the phonon-assisted CR process [$^3P_0$, $^3H_4$] → [$^1G_4$, $^1G_4$] increases with the increase in temperature to some extent. Secondly, the electrons in the $^3P_0$ multiplet populate the nearest low-lying $^1D_2$ multiplet through MPR, and its rate can be estimated using the modified exponential energy gap equation:[32]

$$W_{\mathrm{MPR}}^{(T)} = \beta \exp[-\alpha(\Delta E - 2h\nu_{\max})]\left[1 - \exp\left(-\frac{h\nu}{kT}\right)\right]^{-p} \quad (3)$$

where the constants β and α are 10^7 s^{-1} and 4.5(±1) × 10^{-3} cm,[33] ΔE denotes the energy gap between the initial and final states, $h\nu_{\max}$ represents the highest-vibrational energy in the lattice, p is the number of phonons to bridge the energy gap ($p = \Delta E/h\nu_{\max}$),

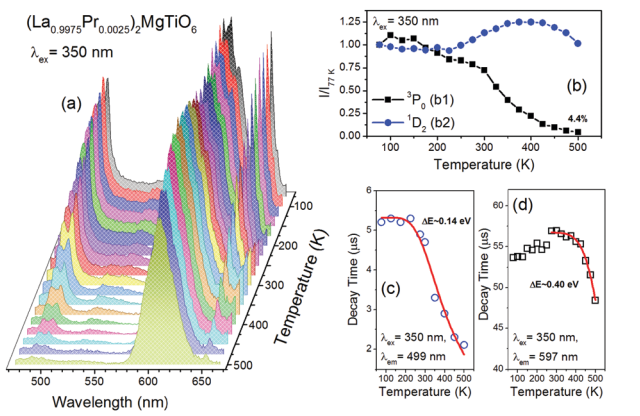

Fig. 9 (a) The emission spectra of $(La_{0.9975}Pr_{0.0025})_2MgTiO_6$ under 350 nm excitation at different temperatures; the temperature-dependent integral intensities of $^3P_0$ (b1) and $^1D_2$ (b2) emissions; and the variations of decay times of (c) $^3P_0$ and (d) $^1D_2$ emissions under IVCT excitation at different temperatures.

and k is the Boltzmann constant (6.958 × 10^{-1} cm^{-1} K^{-1}). Here, ΔE (between $^3P_0$ and $^1D_2$) is ~3866 cm^{-1}, and $h\nu_{\max}$ in La_2MgTiO_6 is ~585 cm^{-1} as shown in Fig. S1 (ESI†). With these parameters, the simulated MPR rate is evaluated to be ~5.4 × 10^2 s^{-1} at 300 K, and it increases to ~1.2 × 10^3 s^{-1} when the temperature rises to 500 K. Nevertheless, this MPR rate at 500 K is still evidently smaller than the A_R of the $^3P_0$ multiplet (2.3 × 10^5 s^{-1}), demonstrating that the contribution of MPR on de-excitation of the $^3P_0$ luminescence is limited in our case. Finally, the influence of electron population from the $^3P_0$ to the [Ti^{4+}–e^-] state through electronic configuration crossover should be emphasized.[19] Reviewing the energy level scheme in Fig. 5(b), the electron in the $^3P_0$ excited multiplet can potentially overcome the energy barrier ΔE_{DC} and back-populate the [Ti^{4+}–e^-] state with the assistance of thermal phonons. By employing the model proposed by Struck and Fonger,[34] the quenching behaviour of $^3P_0$ mainly through this crossover channel can be stimulated by:

$$\frac{I(T)}{I(0)} \sim \frac{\tau(T)}{\tau(0)} = \left(1 + A\exp\left(\frac{\Delta E}{kT}\right)\right)^{-1} \quad (4)$$

where A is the pre-exponential factor and ΔE denotes the required activation energy to promote the electron from its emitting state to the quenching state, k is the Boltzmann constant. Because the luminescence intensity of the activator in the lattice can be easily affected by additional thermally activated non-radiative relaxation effects (for instance, the temperature-dependent oscillator strength and distributed scattering centres)[35] at higher temperatures, we believe that the temperature-dependent decay time of the activator gives a more reliable characterization of thermal-quenching. So, the decay dynamics of $^3P_0$ and $^1D_2$ emissions under the IVCT excitation at different temperatures are shown in Fig. S3 (ESI†), and the variations of decay times of those curves are shown in Fig. 9(c and d). By employing eqn (4), the fitting curve of the $^3P_0$ decay time is exhibited in Fig. 9(c), and the value of ΔE_{DC} is estimated to be ~0.14 eV (1129 cm^{-1}). This value is smaller than those in $Lu_{0.995}Pr_{0.005}NbO_4$ (2490 cm^{-1})[36] and $CaMoO_4$:Pr^{3+} (4100 cm^{-1}),[24] indicating that the de-excitation probability of $^3P_0$ luminescence through this crossover channel is more sensitive to the increase in temperature. Meanwhile, the contributions of phonon-assisted CR and MPR have been included in this fitting process because of the increase in the de-excitation rates of these two channels with the rise in temperature.

The temperature-dependent variation of $^1D_2$ luminescence is quite different from that of $^3P_0$ luminescence. When the temperature increases from 225 to 400 K, an increase in $^1D_2$ luminescence is noticed as shown in Fig. 9(b). The phenomenon implies that some electron population processes become active which enhances the $^1D_2$ luminescence. On the one hand, the increase in the MPR rate from $^3P_0$ to $^1D_2$ would somewhat promote the $^1D_2$ emission intensity at higher temperatures. On the other hand, the depopulating rate of the $^3P_0$ multiplet through the crossover channel rises with the increase in temperature and more electrons transfer to the [Ti^{4+}–e^-] state. After this, these electrons immediately populate the lower-lying $^1D_2$ multiplet (pathway 1 in Fig. 5(b)), and its efficiency increases

remarkably with the rising temperature, leading to a gradual enhancement in $^1D_2$ luminescence intensity. Finally, when the temperature is beyond 400 K, the thermal-quenching behaviour of $^1D_2$ is observed not only in emission spectra but also in decay dynamics. It is evident that the efficiency of the resonant CR channel [$^1D_2$, $^3H_4$] → [$^1G_4$, $^3F_4$] is almost independent of the ambient temperature. Because of the larger energy gap (~6955 cm^{-1}) between the Pr^{3+} $^1D_2$ and $^1G_4$ states, the MPR from $^1D_2$ to $^1G_4$ is also quite inefficient. Therefore, the influence of CR and MPR channels on the de-excitation of $^1D_2$ luminescence is partial in the studied temperature region (77–500 K). We consider that the electronic configuration crossover channel [the $^1D_2$→ the [Ti^{4+}–e^-] state→ the $^3H_4$ ground state] is the main thermal-quenching pathway of $^1D_2$ luminescence. With sufficient thermal phonon assistance at higher temperatures, the electron in the $^1D_2$ multiplet has the potential to transfer to the [Ti^{4+}–e^-] state and finally undergo non-radiative relaxation back to the $^3H_4$ ground state by overcoming the larger energy barrier ΔE_{EF} as displayed in Fig. 5(b). By employing eqn (4), the value of the energy barrier ΔE_{EF} is approximately 0.40 eV (3226 cm^{-1}) as exhibited in Fig. 9(d). Because of the existence of other thermal-quenching channels contributing to the depopulation of the $^1D_2$ multiplet, this ΔE_{EF} value is only an indication of the magnitude of the energy barrier. Nevertheless, the larger value of ΔE_{EF} compared to that of ΔE_{DC} demonstrates indeed that the $^1D_2$ luminescence possesses a better thermal stability in $(La_{0.9975}Pr_{0.0025})_2MgTiO_6$ within a large temperature region.

Because of the differences between the thermal-induced luminescence properties of the $^3P_0$ and $^1D_2$ multiplets, Pr^{3+} doped La_2MgTiO_6 may serve as a possible optical thermometric material. It has been reported that the thermometric characteristics of lanthanide doped materials can be calibrated in several ways: (1) luminescence intensity monitoring;[37] (2) energy maximum shifting of the excitation[38] or emission band[39] with temperature; (3) temperature-dependent emission line width broadening;[40] (4) decay[41] and rising time analysis;[42] and (5) ratiometric emission intensity measurement (RIM).[43] Because of its unique merits, such as self-referencing, the RIM method can eliminate the measurement interference, for example the change in geometry, source intensity, and light field, and has become the most frequently used temperature read-out strategy for optical thermometry.[44,45]

In $(La_{0.9975}Pr_{0.0025})_2MgTiO_6$, the RIM of $^1D_2$–$^3H_4$ (608 nm) and $^3P_0$–$^3H_4$ (499 nm) emissions can be treated as a sensitive temperature probe. The temperature-dependent heights of the sample at 608 and 499 nm emissions under 350 nm excitation are shown in Fig. 10(a). The obtained RIMs at different temperatures are given in Fig. 10(b), showing that the values increase with rising temperatures. The temperature-dependent RIM fit equation[46] in our case is given as:

$$\mathrm{RIM} = \frac{I_{608}}{I_{499}} \sim 1.21 + 260\exp\left(-\frac{0.1295}{kT}\right) \quad (5)$$

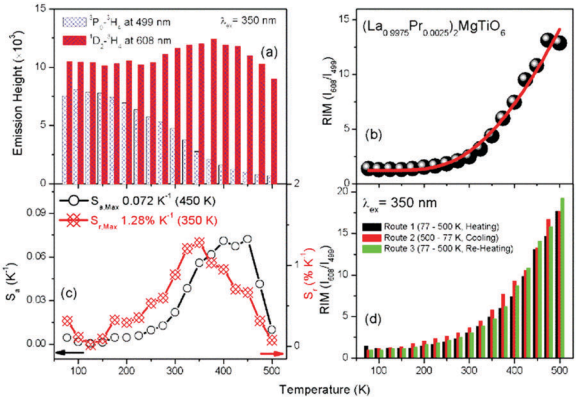

Fig. 10 (a) The temperature-dependent heights of $(La_{0.9975}Pr_{0.0025})_2MgTiO_6$ at 608 and 499 nm emissions under 350 nm excitation; the variations of (b) RIM (I_{608}/I_{499}), and (c) S_a and S_r at different temperatures; (d) the temperature-dependence of RIM (I_{608}/I_{499}) in temperature-recycling measurements.

And, the maximum values of absolute sensitivity (S_a) and relative sensitivity (S_r) are found to be ~0.072 K^{-1} (450 K) and 1.28% K^{-1} (350 K) using eqn (6) and (7):[47]

$$S_a = \left|\frac{\partial \mathrm{RIM}}{\partial T}\right| = C\exp\left(-\frac{E_a}{kT}\right) \times \frac{E_a}{kT^2} \quad (6)$$

$$S_r = 100\% \times \left|\frac{1}{\mathrm{RIM}}\frac{\partial \mathrm{RIM}}{\partial T}\right| = 100\% \times \frac{C\exp\left(-\frac{E_a}{kT}\right)}{B + C\exp\left(-\frac{E_a}{kT}\right)} \times \frac{E_a}{kT^2} \quad (7)$$

as displayed in Fig. 10(c), respectively. The values of these sensitivities in our case are larger than those in $NaYF_4$:Pr^{3+} [48] and compatible with those in Pr^{3+}–Tb^{3+} codoped $NaGd(MoO_4)_2$, $NaLu(MoO_4)_2$, and $NaLu(WO_4)_2$.[49] Moreover, the temperature-recycle measurements were carried out to evaluate the repeatability of this material as presented in Fig. 10(d). It is clear that the RIM values of the sample at a certain temperature during different periods are almost equal to each other. The result shows that the sample has an outstanding repeatability, demonstrating that Pr^{3+} doped La_2MgTiO_6 is a promising candidate for optical thermometry.

4 Conclusion

A Pr^{3+} doped La_2MgTiO_6 material prepared by a high temperature solid-state reaction route exhibits attractive luminescence properties. Rietveld refinement analysis of powder XRD data is performed to confirm its crystal structure. The band gap and the Pr^{3+}–Ti^{4+} ICVT energies are evaluated to be 3.98 and 3.71 eV, respectively. The TRES technique is adopted to distinguish the distributions of $^3P_0$ and $^1D_2$ emissions in the spectrum, and the intense $^3P_0$–$^3F_2$ hypersensitive ED emission line is clearly observed, which is related to the fact that Pr^{3+} ions occupy the La^{3+} sites with obvious deviation from centrosymmetry. A schematic energy level diagram is proposed to illustrate the electron population pathway in Pr^{3+} doped La_2MgTiO_6.

With the increase in the Pr^{3+} doping content, the saturation of light absorptivity on the surface of the sample causes the distinction of excitation intensities of 4f–4f transitions and the IVCT in excitation spectra. The concentration-quenching mechanism of electrons in the $^3P_0/^1D_2$ multiplets is confirmed by employing the Inokuti–Hirayama model. By comparing the concentration-dependent intensities of $^1D_2$ emission under different excitations, we deem that the $^1D_2$ multiplet can be populated through an extra channel under IVCT excitation and concentration-quenching of the $^1D_2$ emission is prior to that of $^3P_0$.

Temperature-dependences of the $^3P_0$ and $^1D_2$ luminescence in our samples follow the distinct variation tendencies. The contributions of different de-excitation channels to the thermal-quenching behaviour of Pr^{3+} luminescence, such as phonon-assisted CR, MPR and the electronic configuration crossover pathway, are discussed in detail. We consider that the sharp decrease in the $^3P_0$ luminescence intensity is mainly induced by electron transfer through the crossover channel between the $^3P_0$ multiplet and the $[Ti^{4+}–e^-]$ state. On the other hand, the $^1D_2$ luminescence possesses an excellent thermal stability in a large temperature region. Since the luminescence intensity of the Pr^{3+} 4f excited multiplet is cooperatively controlled by electron population probability from higher-energy states and electron de-excitation rate to low-lying multiplets, the result reported here gives a general understanding of the relevant electron population mechanism which directly determinates the Pr^{3+} luminescence efficiency in general cases. Finally, the unique temperature sensing properties mean that the Pr^{3+} doped La_2MgTiO_6 material has application potential in the optical thermometry field.

Conflicts of interest

There are no conflicts to declare.

Acknowledgements

The work is financially supported by the National Natural Science Foundation of China (U1432249, 21671201 and U1632101) and the Science and Technology Project of Guangdong Province (2017A010103034).

Notes and references

1 M. Aldén, A. Omrane, M. Richter and G. Särner, *Prog. Energy Combust. Sci.*, 2011, **37**, 422–461.
2 X. D. Wang, O. S. Wolfbeis and R. J. Meier, *Chem. Soc. Rev.*, 2013, **42**, 7834–7869.
3 J. Lou, T. M. Finegan, P. Mohsen, T. A. Hatton and P. E. Laibinis, *Rev. Anal. Chem.*, 1999, **18**, 235–284.
4 D. Jaque and F. Vetrone, *Nanoscale*, 2012, **4**, 4301–4326.
5 C. F. Chan, M. K. Tsang, H. Li, R. Lan, F. L. Chadbourne, W. L. Chan, G. L. Law, S. L. Cobb, J. Hao, W. T. Wong and K. L. Wong, *J. Mater. Chem. C*, 2014, **2**, 84–91.
6 J. Brübach, C. Pflitsch, A. Dreizler and B. Atakan, *Prog. Energy Combust. Sci.*, 2013, **39**, 37–60.
7 Y. Li, J. Wang, X. M. Wang, F. Pan, T. Zhou and R. J. Xie, *J. Mater. Chem. C*, 2017, **5**, 1022–1026.
8 A. Abdukayum, J. T. Chen, Q. Zhao and X. P. Yan, *J. Am. Chem. Soc.*, 2013, **135**, 14125–14133.
9 H. Dong, L. D. Sun and C. H. Yan, *Chem. Soc. Rev.*, 2015, **44**, 1608–1634.
10 P. Boutinaud, R. Mahiou, E. Cavalli and M. Bettinelli, *J. Lumin.*, 2007, **122**, 430–433.
11 G. Liu, *Chem. Soc. Rev.*, 2015, **44**, 1635–1652.
12 J. Suntivich, K. J. May, H. A. Gasteiger, J. B. Goodenough and Y. Shao-Horn, *Science*, 2011, **334**, 1383–1385.
13 A. A. Coelho, *TOPAS Academic V4; Coelho Software*, Brisbane, Australia, 2005.
14 *CRC Handbook of Chemistry and Physics*, ed. W. M. Haynes, 96th edn, CRC Press/Taylor and Francis, Boca Raton, FL, 2016.
15 S. Zhang, H. Liang, C. Liu, Z. Qi, T. Shao and Y. Wang, *Opt. Lett.*, 2013, **38**, 612–614.
16 P. Dorenbos, *ECS J. Solid State Sci. Technol.*, 2014, **3**, R19–R24.
17 P. Liu, J. Nisar, B. Sa, B. Pathak and R. Ahuja, *J. Phys. Chem. C*, 2013, **117**, 13845–13852.
18 V. Kumar, S. K. Sharma, T. P. Sharma and V. Singh, *Opt. Mater.*, 1999, **12**, 115–119.
19 P. Boutinaud, E. Pinel, M. Dubois, A. P. Vink and R. Mahiou, *J. Lumin.*, 2005, **111**, 69–80.
20 C. de Mello Donegá, H. Lambaerts, A. Meijerink and G. Blasse, *J. Phys. Chem. Solids*, 1993, **54**, 873–881.
21 Y. Gao, F. Huang, H. Lin, J. Xu and Y. Wang, *Sens. Actuators, B*, 2017, **243**, 137–143.
22 J. P. M. Van Vliet and G. Blasse, *Chem. Phys. Lett.*, 1988, **143**, 221–224.
23 E. Cavalli, P. Boutinaud, M. Bettinelli and P. Dorenbos, *J. Solid State Chem.*, 2008, **181**, 1025–1031.
24 E. Cavalli, F. Angiuli, P. Boutinaud and R. Mahiou, *J. Solid State Chem.*, 2012, **185**, 136–142.
25 S. Tanabe, T. Hanada, T. Ohyagi and N. Soga, *Phys. Rev. B: Condens. Matter Mater. Phys.*, 1993, **48**, 10591.
26 *Spectroscopic Properties of Rare Earths in Optical Materials*, ed. Liu, G. and Jacquier, B., Springer Science & Business Media, 2006, vol. 83.
27 S. Mahlik, M. Grinberg, E. Cavalli, M. Bettinelli and P. Boutinaud, *J. Phys.: Condens. Matter*, 2009, **21**, 105401.
28 R. Shi, B. Li, C. Liu and H. Liang, *J. Phys. Chem. C*, 2016, **120**, 19365–19374.
29 Z. G. Mazurak, J. P. M. Van Vliet and G. Blasse, *J. Solid State Chem.*, 1987, **68**, 227–233.
30 M. Inokuti and F. Hirayama, *J. Chem. Phys.*, 1965, **43**, 1978–1989.
31 H. Dornauf and J. Heber, *J. Lumin.*, 1980, **22**, 1–16.
32 J. M. F. Van Dijk and M. F. H. Schuurmans, *J. Chem. Phys.*, 1983, **78**, 5317–5323.
33 C. D. M. Donega, A. Meijerink and G. Blasse, *J. Phys. Chem. Solids*, 1995, **56**, 673–685.

34 C. W. Struck and W. H. Fonger, *J. Appl. Phys.*, 1971, **42**, 4515–4516.
35 V. Bachmann, C. Ronda, O. Oeckler, W. Schnick and A. Meijerink, *Chem. Mater.*, 2009, **21**, 316–325.
36 C. Liu, F. Pan, Q. Peng, W. Zhou, R. Shi, L. Zhou, J. Zhang, J. Chen and H. Liang, *J. Phys. Chem. C*, 2016, **120**, 26044–26053.
37 W. H. Fonger and C. W. Struck, *J. Chem. Phys.*, 1970, **52**, 6364–6372.
38 G. Särner, M. Richter and M. Aldén, *Meas. Sci. Technol.*, 2008, **19**, 125304.
39 H. Kusama, O. J. Sovers and T. Yoshioka, *Jpn. J. Appl. Phys.*, 1976, **15**, 2349.
40 A. Benayas, E. Escuder and D. Jaque, *Appl. Phys. B: Lasers Opt.*, 2012, **107**, 697–701.
41 J. Yu, L. Sun, H. Peng and M. I. Stich, *J. Mater. Chem.*, 2010, **20**, 6975–6981.
42 V. Lojpur, Ž. Antić and M. D. Dramićanin, *Phys. Chem. Chem. Phys.*, 2014, **16**, 25636–25641.
43 M. A. Alencar, G. S. Maciel, C. B. de Araújo and A. Patra, *Appl. Phys. Lett.*, 2004, **84**, 4753–4755.
44 K. Zheng, Z. Liu, C. Lv and W. Qin, *J. Mater. Chem. C*, 2013, **1**, 5502–5507.
45 C. D. Brites, P. P. Lima, N. J. Silva, A. Millán, V. S. Amaral, F. Palacio and L. D. Carlos, *Adv. Mater.*, 2010, **22**, 4499–4504.
46 L. H. Fischer, G. S. Harms and O. S. Wolfbeis, *Angew. Chem., Int. Ed.*, 2011, **50**, 4546–4551.
47 L. D. Carlos and F. Palacio, *Thermometry at the Nanoscale: Techniques and Selected Applications*, Royal Society of Chemistry, 2015, vol. 38.
48 S. Zhou, G. Jiang, X. Wei, C. Duan, Y. Chen and M. Yin, *J. Nanosci. Nanotechnol.*, 2014, **14**, 3739–3742.
49 Y. Gao, F. Huang, H. Lin, J. Zhou, J. Xu and Y. Wang, *Adv. Funct. Mater.*, 2016, **26**, 3139–3145.